RSC Advances

PAPER

View Article Online
View Journal | View Issue

Cite this: *RSC Adv.*, 2024, **14**, 11429

Exploring the thermal decomposition and detonation mechanisms of 2,4-dinitroanisole by TG-FTIR-MS and molecular simulations†

Nian Yang,[a] Tianlong Wu,[a] Xiaofang Bao,[a] Teng Ma,[a] Yinsheng Huang,[a] Dabin Liu,[a] Xuedong Gong,[a] Yan A. Wang,[b] Sen Xu*[a] and Baojing Zhou *[a]

2,4-dinitroanisole (DNAN), an insensitive explosive, has replaced trinitrotoluene (TNT) in many melt-cast explosives to improve the safety of ammunition and becomes a promising material to desensitize novel explosives of high sensitivity. Here, we combine thermogravimetric-Fourier transform infrared spectrometry-Mass spectrometry (TG-FTIR-MS), density functional theory (DFT), and ReaxFF molecular dynamics (MD) to investigate its thermal decomposition and detonation mechanisms. As revealed by TG-FTIR-MS, the thermal decomposition of DNAN starts at *ca.* 453 K when highly active NO_2 is produced and quickly converted to NO resulting in the formation of a large amount of $Ph(OH)(OH_2)OCH_3^+$. DFT calculations show that the activation energy of DNAN is higher than that of TNT due to the lack of α-H. Further steps in both thermal decomposition and detonation reactions of the DNAN are dominated by bimolecular O-transfers. ReaxFF MD indicates that DNAN has a lower heat of explosion than TNT, in accordance with the observation that the activation energies of polynitroaromatic explosives are inversely proportional to their heat of explosion. The inactive $-OCH_3$ group and less nitro groups also render DNAN higher thermal stability than TNT.

Received 2nd February 2024
Accepted 27th March 2024

DOI: 10.1039/d4ra00860j

rsc.li/rsc-advances

1. Introduction

Nitro-aromatic compounds are important energetic materials that are widely used in many military and civilian applications.[1–11] Among them, 2,4-dinitroanisole (DNAN) is an insensitive melt-cast matrix ingredient, which was used to prepare Amatol-40 explosives in WWII.[11,12] Since the 1980s, DNAN has again aroused strong attention and has become a promising energetic material to replace the traditional trinitrotoluene (TNT) in melt-cast explosives to make them less sensitive[13–19] owing to its kinetic inertness and thermal stability. Various DNAN-based melt-pour explosive formulations have been developed[20–32] and put into service.[33–35] However, researchers have identified several drawbacks and challenges related to the physical properties, sensitivity, stability, compatibility, and oxygen balance of DNAN, which could potentially hinder its future applications.[36] Therefore, a comprehensive understanding of the characteristics of DNAN is essential to solve various problems caused by its use.

In the past decade, the heat capacity, thermal behavior, and thermal hazards of DNAN have been investigated by many research groups.[37–44] Researchers studied the thermal decomposition behavior of DNAN using accelerated calorimetry (ARC) and differential scanning calorimeter (DSC). The activation energies (E_a) of DNAN calculated from ARC data is 61.91 kcal mol^{-1},[40] and that measured by DSC and ARC under adiabatic conditions is 71.19 kcal mol^{-1}.[41] These data indicate that DNAN exhibits greater kinetic inertness and thermal stability compared to TNT and enable researchers to predict the stability and safety of DNAN-based melt-cast explosives. It is unsurprising that the use of DNAN to desensitize novel emerging sensitive high-energy density explosives has become very promising.[27,45–51]

On the other hand, the Evans–Polanyi–Semenov (E–P–S) equation[52–56] describes a relationship between activation energies (E) of many radical reactions and their heats of reaction (ΔH): $E = B + \alpha'_* \Delta H$, where B is a constant and can be viewed as a measure of how far a reaction has proceeded along the reaction coordinate when the transition state (TS) is reached. Based on the EPS equation, it was found that for polynitroaromatics, such as TNT and TATB, the activation energy for thermal decomposition is inversely proportional to the heat of detonation.[57] It can be used to explain the chemical micromechanism governing between thermal decomposition and detonation of DNAN, a kind of polynitroaromatics.

[a]*School of Chemistry and Chemical Engineering, Nanjing University of Science & Technology, Nanjing 210094, China. E-mail: xusen@njust.edu.cn; bzhou@njust.edu.cn*

[b]*Department of Chemistry, University of British Columbia, Vancouver, British Columbia V6T 1Z1, Canada*

† Electronic supplementary information (ESI) available. See DOI: https://doi.org/10.1039/d4ra00860j

The thermal decomposition mechanism of DNAN cannot be adequately understood without analyzing its thermal decomposition intermediates and products. To gain insight into the detailed thermal decomposition mechanism of energetic materials, researchers have employed a range of analytical techniques, including thermogravimetric analysis (TG), Fourier transform infrared spectrometry (FTIR), and mass spectrometry (MS), to analyze the evolved gaseous intermediates and products.[58–67] In 2014, Maharrey *et al.*[67] used simultaneous thermogravimetric modulated beam mass spectrometry to explore the thermal decomposition process of DNAN. The decomposition onset was measured to be 483 K. Their results suggested that the first step is the melting of DNAN, followed by the equilibrium evaporation of liquid DNAN. Later, 2,4-dinitrophenol is formed from DNAN through a rearrangement reaction involving an H transfer from C to O in the $-OCH_3$ group and the subsequent release of CH_2. In 2015, Liu *et al.*[58] proposed a dynamic pressure-measuring thermal analysis (DPTA) techniques to evaluate the thermal stability of energetic materials. They combined DPTA, MS, and density functional theory (DFT) calculations to study the thermal decomposition of three volatile low-melting explosives, *i.e.* TNT, DNAN, and 3,4-bis(3-nitrofurazan-4-yl)furoxan (DNTF). The results suggested that DNAN has the best thermal stability, while DNTF is the most heat-sensitive. In 2021, Wojtas *et al.*[63] combined DSC with thermally enhanced Fourier-transform infrared spectroscopy to analyze the entire process of thermal decomposition of DNAN. DNAN was stable in the liquid phase up to 423 K, and the fastest thermal decomposition rate was detected at 613 K, and the gas products measured during the thermal decomposition of DNAN were mainly CO, CO_2, N_2O, and CH_3OH.

Despite the efficiency of the aforementioned measurements,[58,63,67] the information they provided was still limited because many reaction intermediates cannot be detected due to their short lifetime and trace amounts. Thus, the results are insufficient to establish a detailed thermal decomposition mechanism and detonation of DNAN convincingly at the molecular level. The combination of TG-FTIR-MS with molecular simulations turns out to be a useful tool for this purpose. In the last decade, reaction force field (ReaxFF) molecular dynamics (MD) simulations[68–85] have been widely used to obtain detailed information for reaction processes at the molecular level beyond measurements.

In the present study, we combine ReaxFF MD and DFT calculations with TG-FTIR-MS analysis to investigate the thermal decomposition and detonation mechanisms of DNAN. TG-FTIR-MS is used to identify the products generated from the initial thermal decomposition of DNAN under mild conditions. Based on the measured data, a thermal decomposition mechanism of DNAN is proposed and further rationalized by our DFT calculations. ReaxFF MD simulations are also performed to investigate the detonation process of DNAN. Based on the experimental and computational results, the major reaction pathways as well as key kinetic parameters of DNAN thermal decomposition and detonation are obtained. Moreover, the relationship between the thermal decomposition and detonation mechanisms of DNAN is analyzed.

2. Methods

2.1 Experiments section

DNAN produced by Alfa Aesar, with a purity above 98%, was dried at 348 K for one day before experiments. TG-FTIR-MS tests were carried out to analyze the species of products in gas phase during the entire thermal decomposition process of DNAN in the temperature range of 308–683 K. These tests consist of the following parts: a TG-DTA instrument (ErkinElmer STA8000), an FTIR spectrometer (ErkinElmer Spectrum 3) and a GC-MS instrument (Clarus SQ 8 GC-MS). The reaction vessel was first heated to 308 K, then approximately 5 mg samples were loaded into an open aluminum pan and heated to 683 K at 5 K min^{-1} under a nitrogen flow at 20 ml min^{-1}. The spectra of the evolution of gas fragments during the thermal decomposition of DNAN were recorded by an FTIR spectrophotometer in real-time tracking mode with a scan range of 4000 cm^{-1} to 500 cm^{-1} at a resolution of 2 cm^{-1}. The *m*/*z* for gas-phase fragments evolution during DNAN decomposition was recorded by the mass spectrometer conducting the dynamic scanning in the *m*/*z* range from 1 to 400.

2.2 Computational methods

The thermal decomposition processes of DNAN are studied using DFT calculations, while ReaxFF-lg MD calculations simulate its detonation. The temperature is set to 500 K in DFT calculations in accordance with the TG-FTIR-MS analysis. DFT calculations are also performed to compare the potential energy (PE) barrier of key reactions. The *NVT* ensemble is employed for ReaxFF-lg MD simulations at 2500 K and 3500 K to ensure the detonation of DNAN is complete.

2.2.1 DFT calculations. DFT calculations were carried out to estimate the thermodynamic parameters, *i.e.* enthalpy and Gibbs free energy changes, for some key reaction pathways. The calculations were performed using the Gaussian09 package[86] and the M062X-D3 (ref. 87) density functional in conjunction with the 6-311+G(d,p) basis set were used. The vibrational analysis was performed at the same level of theory to reliably characterize the optimized structures either as the local minima or TS. Intrinsic reaction coordinates (IRC) calculations were performed to examine whether the TS under consideration connected the expected reactants and products properly.

2.2.2 ReaxFF-lg MD simulations. In this study, we use the large-scale atomic/molecular massively parallel simulator (LAMMPS) to perform the ReaxFF-lg MD simulations.[69,76–78] The force field parameters of DNAN are obtained from the report by Liu *et al.*[76] The crystal structures of DNAN and TNT belong to the monoclinic system with the space group *P*21/*n* and orthorhombic system with the space group *Pca*21, respectively (Fig. 1). Their lattice parameters from the X-ray diffraction are provided in Table S1†.[79,80] The optimized cell parameters and densities of the DNAN and TNT unit cells by the ReaxFF-lg agree well with experimental data within less than 5% deviation (Table S1†). The bond lengths of DNAN and TNT by ReaxFF-lg and DFT agree well with the experimental data[79,80] (Table S2†).

The following fast-heating protocol is employed to compare the thermal sensitivity of DNAN and TNT. First, an internal

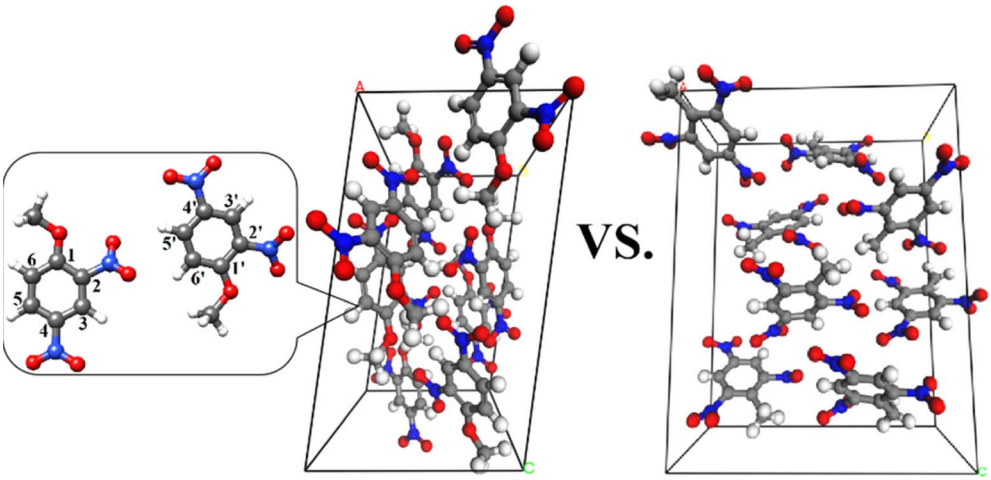

Fig. 1 The unit cell of DNAN (left) and TNT (right). The C, H, O, and N atoms are colored gray, white, red, and blue, respectively.

pressure relaxation for the crystal unit cells was performed for 10 ps with an isothermal-isobaric (*NPT*) ensemble at 300 K and 0 Pa. Then, DNAN and TNT unit cells were quickly heated to 2500 K in 2 ps. Afterward, the two systems evolve under the canonical (*NVT*) ensemble for 100 ps.

A slow-heating protocol is employed to simulate the detonation process of DNAN at 2500 K and 3500 K, respectively, for which a $2 \times 4 \times 1$ supercell of 1.56 g cm^{-3} was used. First, the system was relaxed at 300 K and 0 Pa for 10 ps with the *NPT* ensemble, after which its equilibrium density slightly decreased to 1.53 g cm^{-3}. Then, the system was slowly heated to the set temperature of 50 ps. Finally, the system evolves under the *NVT* ensemble at the two temperatures for 500 ps and 250 ps, respectively. In MD simulations, the time step was set to 0.1 fs to effectively cover the phase space and allow the collisions and reactions to occur smoothly. Snapshots along the MD trajectories were recorded every 100 fs. These collected data were analyzed using Findmole[81] and in-house programs to extract information about chemical reactions during the process.

2.3 Kinetic analysis

The thermal decomposition process of DNAN is divided into three stages. The initial and intermediate stages are separated at t_{max}, when the PE reaches the maximum.[61,83,86] For the intermediate stage, the following linear form of the Arrhenius equation is used to describe the reaction kinetics,

$$\ln(k) = \ln(A) - \frac{E_a}{RT}, \quad (1)$$

where k is the rate constant, A is the pre-exponential factor, E_a is the activation energy, R is the universal gas constant, and T is the temperature. The rate constant for reactions in the second stage (k_1) is fitted with an exponentially decaying function,

$$U_t = U_\infty + (U_{max} - U_\infty)\exp[-k_1(t - t_{max})], \quad (2)$$

where U_t is the value of PE at moment t, U_∞ is the asymptotic value of PE, U_{max} is the maximum PE. The kinetic parameters A and E_a in eqn (2) are determined from the rate constants k's at 2500 and 3500 K.

In the final stage, the reaction slows down compared to the intermediate stage, and the amounts of final products, *i.e.* H_2O, N_2, CO_2, and H_2, steadily increase. The rate constant for reactions in the final stage (k_2) can be calculated for each product by fitting the following function,

$$C_t = C_\infty\{1 - \exp[-k_2(t - t_i)]\}, \quad (3)$$

where C_∞ is the asymptotic amount of the ith product, t_i is the moment of its earliest formation.

3. Results and discussion

Here, we first discuss the thermal decomposition of DNAN, followed by its detonation in the condensed phase, and finally compare the key reactions that occurred in them.

3.1 DNAN thermal decomposition

3.1.1 Products from DNAN thermal decomposition. The various fragments produced by DNAN thermal decomposition were simultaneously detected by TG coupled with FTIR. The 3D diagrams of the infrared spectrum for gas-phase fragments evolution are shown in Fig. 2(a). No absorption bands can be distinguished before 459 K, indicating that DNAN does not decompose before 459 K. Then, absorption bands reach the maximum at 510 K, and several noticeable absorption bands can be distinguished.

FTIR spectral region in the 500–3500 cm^{-1} of the evolved products at the selected temperatures (459 K, 510 K, 546 K) during the thermal decomposition of DNAN are shown in Fig. 2(b). Several noticeable absorption bands are attributed to the gas phase vibrations of NO, NO_2, CH_3OH, and benzene. The peaks at 3095 cm^{-1}, 1020 cm^{-1}, 915 cm^{-1}, 1609 cm^{-1}, and 1494 cm^{-1} are assigned to C–H stretching, C–H bending, and C=C stretching of benzene, respectively. The absorption peak at 2950 cm^{-1} signals NO. The vibration of NO_2 produces two

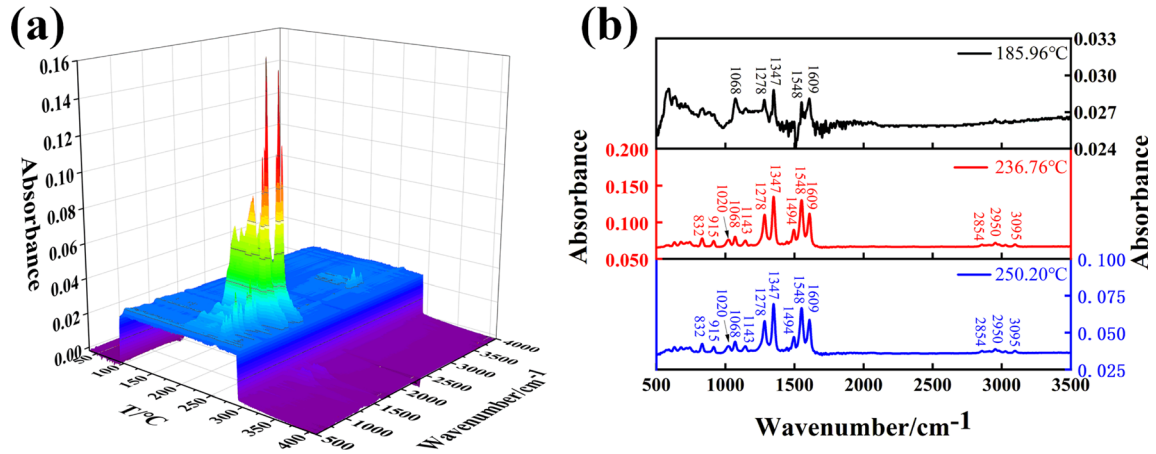

Fig. 2 3D diagrams of infrared spectrum for gas-phase fragments evolution (a) and FTIR in the 500–4000 cm^{-1} spectral region of the evolved products at the selected temperatures (b) during the DNAN thermal decomposition.

absorption bands at 1548 cm^{-1} (antisymmetric stretching) and 1347 cm^{-1} (symmetric stretching). The absorption peak at 1143 cm^{-1} is assigned to CH_3OH. The absorption peak at 2854 cm^{-1} is assigned to the C–H stretching of the methyl group. The absorption peaks at 1280 cm^{-1}, 834 cm^{-1}, and 1068 cm^{-1} are assigned to the N–O and C–O stretching of the functional group –C–O–NO_2. Further MS analysis was performed to identify the gas products and volatile compounds from the thermal decomposition of DNAN.

The gas phase products were simultaneously detected by GS-MS followed by TG-FTIR, and the evolutions of the intensity of the main gas products are shown in Fig. 3. As shown in Fig. 3, some remarkable characteristic peaks (m/z = 30, 46, 107, 127, 141 and 142) are visible. Combined with the absorption peaks in the FTIR, the peaks with m/z of 30 and 46 are assigned to NO (m/z = 30) and NO_2 (m/z = 46), respectively. Three heavier compounds containing the benzene moiety (m/z = 107, 127, 141, and 142) are also produced. It can be found from Fig. 3 that NO is not produced before 455 K and reaches its maximal concentration at 601 K. Then, this is accompanied by the appearance of $Ph(OH)(OH_2)OCH_3^+$ (m/z = 141/142) at 460 K, with a maximum at 530 K. Clearly, $Ph(OH)(OH_2)OCH_3^+$ is the dominant species in the gas products exhibiting the highest intensity. Later at 465 K, another major species in the gas products, $Ph(OH)_2$–OH_2^+ (m/z = 127), is produced and peaks their maximum at 530 K. Finally, trace amounts of NO_2 (m/z = 46) and $PhOCH_3$ (m/z = 107) appear at 510 K and 554 K, respectively. Note that the protons in various species detected by GS-MS are from DNAN molecules under thermal decomposition since we used the traditional electron impact ionization method, which produces no proton.

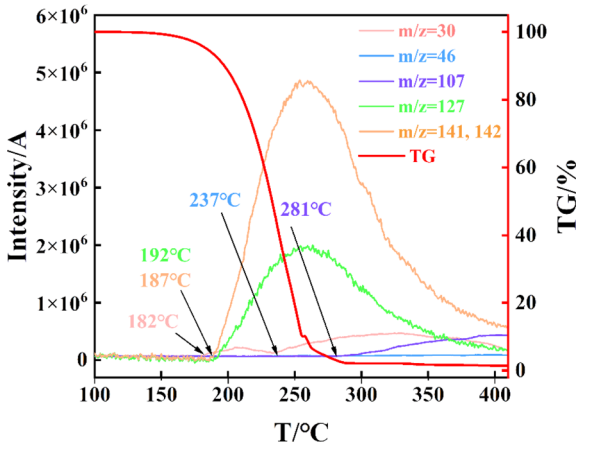

Fig. 3 Evolutions of the intensity of main gas products: NO (pink), NO_2 (blue), $Ph(OH)_2$–OH_2^+ (violet), $Ph(OH)(OH_2)OCH_3^+$ (orange), $PhOCH_2^-$ or $Ph^-{\cdot}OCH_3$ (green).

3.1.2 Thermal decomposition mechanism of DNAN. Based on the TG-FTIR-MS results, the following reaction schemes are proposed for the initial thermal decomposition of DNAN (Fig. 4). At the beginning, highly active NO_2 is produced, but is not detected since it is quickly converted to NO. This results in the formation of a large amount of $Ph(OH)(OH_2)OCH_3^+$ (Fig. 4 and Scheme 1). Most of them were detected, although a small amount further decomposed to CH_2O and $Ph(OH)_2OH_2^+$ (Fig. 4 and Scheme 2) in the condensed phase. Subsequently, CH_3O^+ loses its H successively to decompose to CH_2O and CHO^+. Scheme 1 is the major reaction and the nitro group is more reactive than the methoxy group. Finally, trace amounts of DNAN decompose to NO_2 and Ph^-–OCH_3 (Fig. 4 and Scheme 3) at a higher temperature.

Previous experimental studies and molecular simulations have revealed some basic mechanisms that govern the decomposition of nitroaromatic explosives such as TNT and TATB.[76–80,86–90] Four major routes were reported as the initiating agents of detonation: (1) C–N bond homolytic cleavage to generate NO_2,[76–80] (2) nitro (–NO_2) isomerization rearrangement to form nitrite (–ONO) followed by the O–NO bond breaking to form NO,[88–92] (3) intra- (α-) and intermolecular H transfer,[68,87,88,90–93] (4) intermolecular O transfer.[93]

The major unimolecule reactions, that initiate the thermal decomposition of DNAN, are summarized in Fig. 5(a). Previous studies suggest that the triggering reaction is the homolysis of

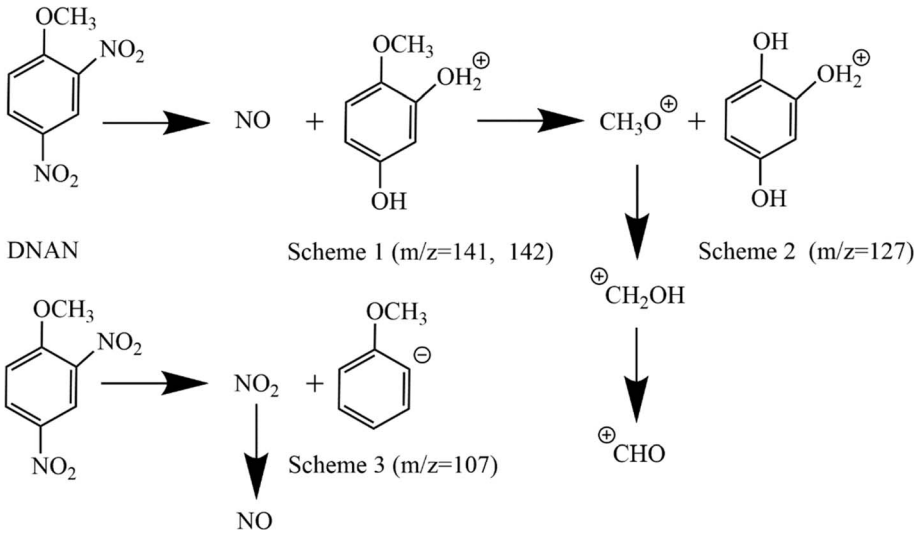

Fig. 4 The proposed reaction schemes for the initial thermal decomposition of DNAN based on the TG-FTIR-MS data.

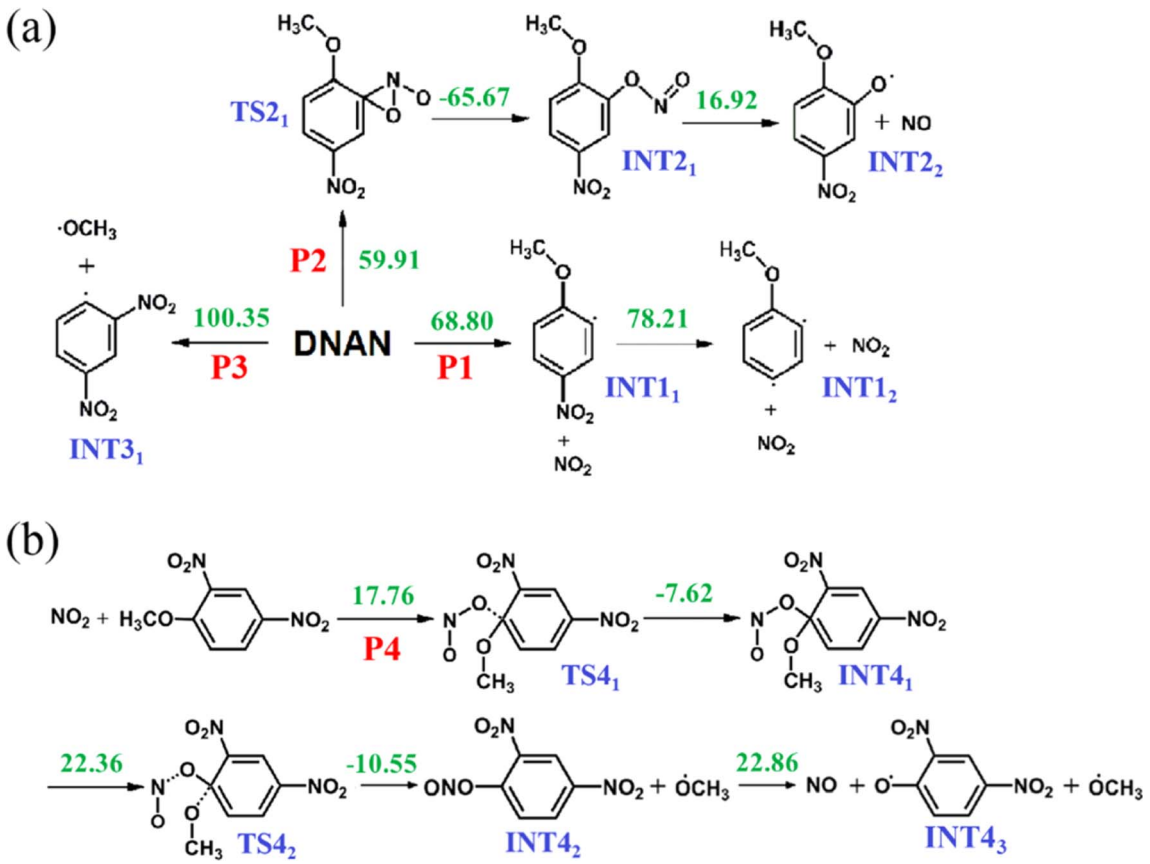

Fig. 5 (a) Major unimolecular reaction paths (P1 to P3) and (b) bimolecular reaction path (P4) during the decomposition of the DNAN. Numbers in green are enthalpy changes of each step at 500 K (kcal mol^{-1}) calculated from DFT.

the *ortho*-C–NO_2 bond (P1), which is endothermic, and DFT calculations show that ΔH is 68.80 kcal mol^{-1} at 500 K. The homolysis of the remaining *para*-C-NO_2 bond requires much more heat (ΔH = 78.21 kcal mol^{-1}). This explains why only a very small amount of Ph–OCH_3 is detected by our TG-FTIR-MS experiment at a higher temperature of *ca.* 554 K (Fig. 3). Another key unimolecular route is the C–NO_2 rearrangement (P2). The TS ($TS2_1$) contains a triangular C–N–O ring. The breaking of the C–N bond in $TS2_1$ leads to the formation of $INT2_1$. Subsequent O–NO bond homolysis in $INT2_1$ produces NO and $INT2_2$. The

third unimolecular path, *i.e.* the homolysis of the C–OCH_3 bond, is more difficult for DNAN (P3) since more heat is required for this reaction ($\Delta H = 100.35$ kcal mol^{-1}). The p–π conjugation between the O atom and the phenyl ring strengthens the C–OCH_3 bond. This path causes the formation of $^{\bullet}OCH_3$ and $INT3_1$. The $^{\bullet}OCH_3$ radical is further dehydrogenated to form HCHO. Note that the overall enthalpy changes for these three unimolecular reaction paths are all positive and they produce highly active radicals for later reactions.

In our TG-FTIR-MS experiment, $Ph(OH)_2$–OH_2^+ is detected, indicating an O transfer should occur at C_{OCH3} of DNAN. DFT calculations suggest that highly active NO_2 can attack the C_{OCH3} atom to form $TS4_1$ (Fig. 5(b), P4). Then, $TS4_1$ turns to its more unstable tautomer, $TS4_2$, *via* $INT4_1$. The C–OCH3 bond is now effectively activated. Further release of the –OCH_3 group from $TS4_2$ results in the formation of $INT4_2$, which decomposes to NO and $INT4_3$. Thus, in this environment, NO_2 is a highly active radical and reacts quickly with DNAN and other species to be reduced to NO.

We calculated the enthalpy changes (ΔH) of each step (Fig. 5) and the relative Gibbs free energies (Table 1) of the involved species for the initiating reactions at 500 K through DFT. The energy barrier ($\Delta H = 17.76$ kcal mol^{-1}) of P4 is much smaller than those initiating reactions, so P4 is expected to be a route of high frequency, which explains why NO is detected earlier (at *ca.* 408 K) and in larger quantities than NO_2 in our TG-FTIR-MS analysis (Fig. 3). Moreover, $^{\bullet}OCH_3$ mainly departs from the benzene ring through P4 instead of P3.

3.2 Detonation of DNAN in condensed phase

In the condensed phase, DNAN bimolecular reactions are facilitated by the proximity of neighboring molecules. The phenyl ring of DNAN is positively charged due to the electron-withdrawing substituents. Thus, the nitro oxygen atom can attack the carbon of the phenyl ring leading to nucleophilic substitutions. There are three types of reaction sites for intermolecular O transfer on the phenyl ring, *i.e.* C2 and C4, C1, and C3, C5 and C6 (Fig. 1).

3.2.1 Detonation of DNAN *vs.* TNT during fast heating. We compare the thermal sensitivities and detonation properties of DNAN and TNT in the condensed phase using the fast-heating protocol outlined in 3.1. The PE of both systems spikes due to the fast heating as the temperature increases from 300 K to 2500 K (Fig. S1†). Under the same temperature conditions, the PE of TNT reaches the maximum earlier than that of DNAN. Naturally, TNT decomposes before DNAN does. Afterward, a steeper decrease in PE is predicted for TNT than for DNAN, suggesting a more violent decomposition in the TNT crystal. Previous studies[87] have shown that TNT in the condensed phase mainly undergoes bimolecular H transfer reaction, and analysis of the TNT MD trajectory shows that the number of H transfer reactions is three times greater than that of O transfer reactions (Fig. S2†).

In contrast, the lack of α-H in DNAN hinders its activation, while its contains only two NO_2 causes severe negative O balance and the oxidation of C, H, and N is inadequate in the later stage. Furthermore, in DNAN, the C_{ph}–O–C bond angle is 120° (Fig. 1), indicating sp^2 hybridization for the O in the methoxyl group. The p–π conjugation renders –OCH_3 in DNAN higher stability and lower reactivity. Consequently, the bimolecular H transfer reaction is more difficult and suppressed during the thermal decomposition of DNAN. These factors to some extent explain the lower thermal sensitivity of DNAN than that of TNT.

3.2.2 Detonation mechanism of DNAN during slow heating. We further use the slow-heating protocol outlined in 3.1 to simulate the thermal decomposition of DNAN at 2500 K and 3500 K, respectively. The evolution of the PE and the total number of DNAN (n_{DNAN}) in the supercell are shown in Fig. 6. In the first stage, the PE increases rapidly with the temperature. When the set temperature (2500 K or 3500 K) is reached at 60 ps,

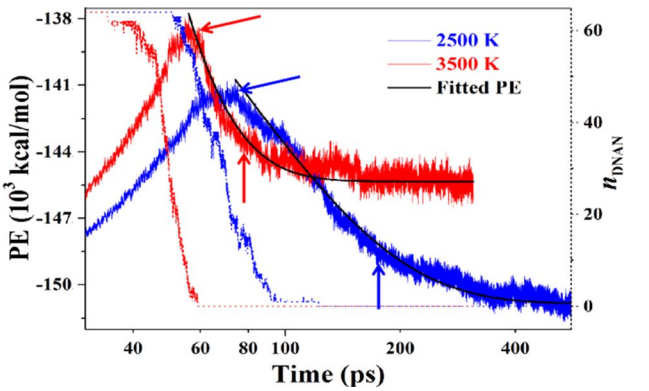

Fig. 6 The evolution of the PE (solid lines) and n_{DNAN} (dashed lines) during the decomposition of DNAN under the *NVT* condition at 2500 K (blue) and 3500 K (red). Black lines are the exponential fit of the PE. The arrows indicate the separation of the three decomposition stages.

Table 1 Major species involved in the initial thermal decomposition paths of DNAN and their Gibbs free energies relative to a DNAN (P1, P2, P3) or NO_2 and DNAN (P4) at 500 K (kcal mol^{-1}).[a]

Path	Gibbs free energy
P1	$INT1_1$ + NO_2 (45.68), $INT1_2$ + $2NO_2$ (102.11)
P2	$TS2_1$ (59.92), $INT2_1$ (−7.17), $INT2_2$ + NO (−10.13)
P3	$INT3_1$ + OCH_3 (77.55)
P4	$TS4_1$ (46.21), $INT4_1$ (38.28), $TS4_2$ (59.27) $INT4_2$ + OCH_3 (28.12), $INT4_3$ + NO + OCH_3 (31.13)

[a] Note that in DNAN, the –OCH_3 and *ortho*-NO_2 adopt opposite orientations (Fig. 1) and are too far away for intramolecular H transfer. In contrast, both intra- and intermolecular H transfers were reported in the thermal decomposition of TNT[80–83] and the former, *i.e.* the α-H transfer is the triggering reaction.

the PE is almost at its maximum and the energy absorbed by DNAN is already above the activation energy for its thermal decomposition. Thus, a significant number of DNAN molecules have decomposed. In the second stage, the decomposition continues and a lot of heat is rapidly released. Clearly, the rate of decomposition is faster at 3500 K than at 2500 K and so does the rate of PE drop. In the third stage, the rate of decomposition drastically decreases and the PE curve plateaus, approaching chemical equilibrium. At 3500 K, the higher stable value of PE at the end compared to that at 2500 K is mainly due to the more complete decomposition of DNAN leading to more small fragments and less chemical bonds and larger deformation of product molecules and clusters.

The numbers of direct bonding between C, H, O, and N atomic pairs during the decomposition of DNAN are summarized in Fig. S3.† Carbon is oxidized because the amount of C–H bonds gradually decreases, while the amount of C–O bonds increases. The amount of O–N bonds gradually decreases and that of N–N bonds increases, indicating that nitrogen is reduced. The amounts of O–H and H–H bonds keep increasing proving that H is partially oxidized. More N_2 is produced at 3500 K than at 2500 K at the end since a higher temperature causes more N atoms to escape from the carbon cluster product. A higher temperature also favors the breaking of C–H bonds, leading to more H$^{\bullet}$ radicals and H_2, which can reduce more NO*x* to N_2.

3.2.2.1 Initial decomposition stage. All reactions involving at least one complete DNAN at the initial decomposition stage are summarized in Table 2. These reactions are classified into three categories. The first category includes three types of unimolecular reactions (P1, P2, P3) as discussed in 4.2.1. The second category includes reactions between two DNAN molecules (referred to as reaction A + A), while the third category contains reactions between a DNAN molecule and another active fragment radical produced from primary reactions (referred to as reaction A + B). Reactions A + B include O transfer and H transfer reactions. The former is similar to O transfer between two DNAN (P5-7), while the latter is similar to H transfer between two DNAN (P8). Note that more than 50% of DNAN molecules undergo A + B reactions in the third category at both temperatures.

In the condensed phase, about 25% of DNAN molecules undergo unimolecular reactions in the early stage. The frequency of unimolecular reactions decreases as: P1 > P3 > P2 (Fig. 5(a)). The remaining 75% of initial reactions are bimolecular. At both temperatures, the number of O transfer reactions is greater than that of H transfer reactions. At higher *T*, the number of O transfers increases, while that of H transfer decreases, indicating a competition between the two types of reactions and a lower reaction barrier for the latter. At both temperatures, the C–NO_2 homolysis occurs first, followed by the O transfer reaction. The chronological order of bimolecular reactions at 2500 K is shown in Fig. S4.†

The four types of A + A biomolecule reactions (P5–8) are summarized in Fig. 7. The frequencies of O transfer reactions decrease as P5 > P6 ≥ P7. The nitro oxygen prefers to transfer to C_{NO_2} (P5). The nitro group at C4′ rotates to approach C2, forming $INT5_1$, whose C–NO_2 bond is effectively activated. Thus, NO_2 is released from $INT5_1$, and $INT5_2$ is produced, which further breaks apart into $INT5_3$, $INT5_4$, and NO_2. In contrast, the transfer of nitro O to C1 (P6), which is less favorable due to the p–π conjugation between –OCH_3 and the phenyl ring, leads to the formation of $INT6_1$. Further release of the –OCH_3 group from $INT6_1$ leads to the formation of $INT6_2$ and $OCH_3^{\bullet}$ radicle, which is an endothermic process. Then, $INT6_3$ and $INT6_4$ can be formed from the dissociation of $INT6_2$. The third type of oxygen transfer pathway involves the transfer of the nitro O to C3, C5, or C6 (P7), which produces $INT7_1$. The connection bridge of $INT7_1$ breaks to yield $INT7_2$ and $INT7_3$.

As to the bimolecular H transfer (P8), the nitro O at C2 of one DNAN adsorbs the H atom from the –OCH_3 group of the adjacent DNAN to form $TS8_1$ containing a five-membered C–H–O–N–O ring. Then, $TS8_1$ relaxes to its more stable tautomer, $INT8_1$. The newly formed weak C–O bond in the connection bridge of $INT8_1$ breaks to yield $INT8_2$ and $INT8_3$. The breaking of the C1′–OCH_2 bond in $INT8_2$ and the N–OH bond in $INT8_3$ leads to the formation of HCHO molecules and OH$^{\bullet}$ radicles. Afterwards, OH$^{\bullet}$ combines with H$^{\bullet}$ to produce H_2O.

In the A + B bimolecular reactions, a DNAN reacts with its various fragments produced from primary reactions, which also include O transfer and H transfer reactions. As the temperature

Table 2 The initial time and frequency of the initial decomposition paths for condensed phase DNAN under *NVT* conditions at 2500 K and 3500 K

	2500 K		3500 K	
Reaction	$t_{initial}$ (ps)	Frequency	$t_{initial}$ (ps)	Frequency
Unimolecular	53.4	16	40.0	17
C–NO_2 homolysis (P1)	53.4	11	40.0	12
C–NO_2 rearrangement (P2)	62.8	2	49.4	1
C–OCH_3 homolysis (P3)	60.2	3	47.6	4
Bimolecular (A + A)	56.8	8	43.2	5
O transfer (P5–7)[a]	56.8	6	43.2	4
H transfer (P8)	60.2	2	50.6	1
Bimolecular (A + B)	57.2	32	44.2	37
O transfer	57.2	15	44.2	30
H transfer	58.2	17	47.8	7

[a] The frequencies of three types of A + A bimolecular oxygen transfer reactions (P5–7) are 3,2,1 and 2,1,1 at 2500 K and 3500 K, respectively.

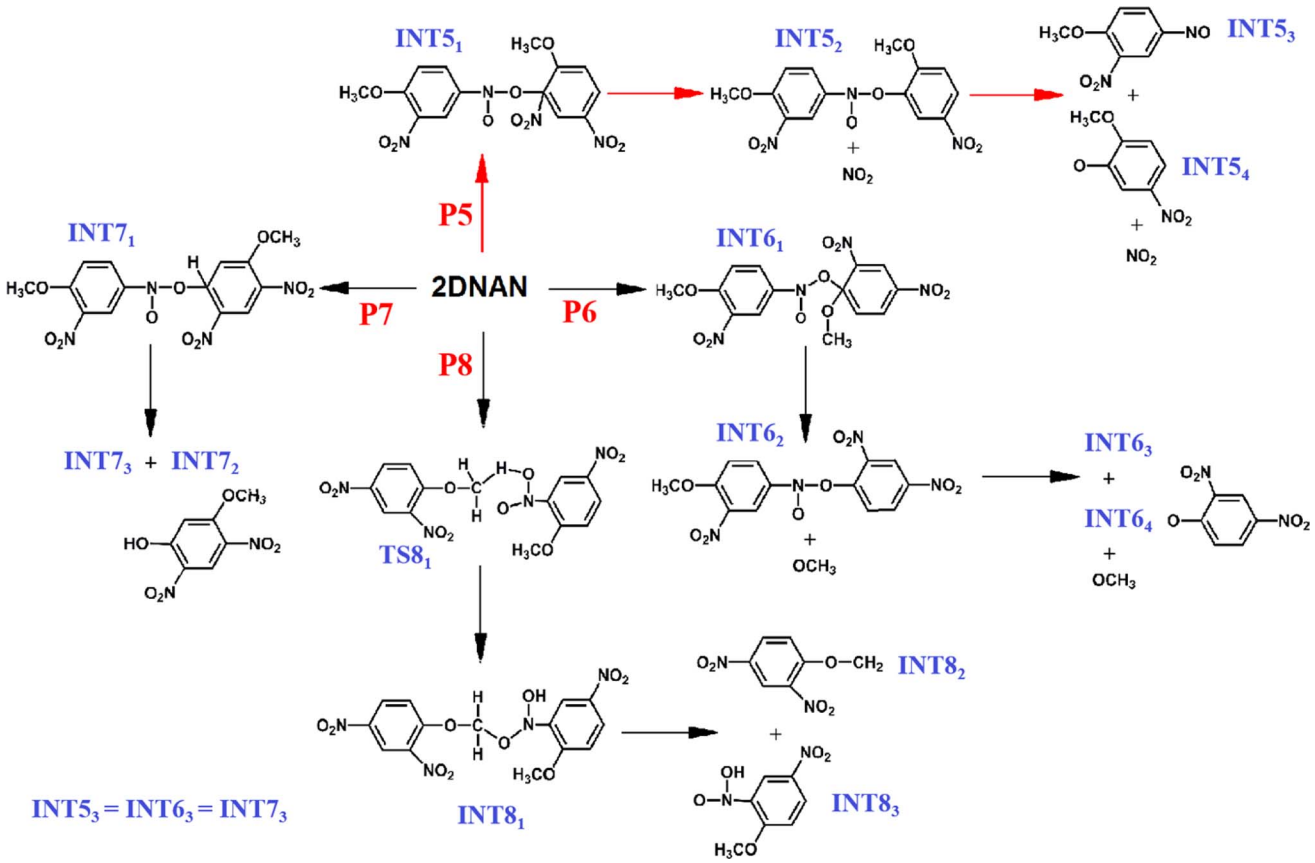

Fig. 7 Major bimolecular reaction paths and intermediate species during the initial thermal decomposition of condensed phase DNAN. P5, P6, and P7 are three bimolecular O transfer reactions, while P8 is a bimolecular H transfer reaction.

increases from 2500 K to 3500 K, the frequency of A + B bimolecular reactions increases significantly (Table 2) because more fragments and radicals like NO_2 of higher mobility are produced to facilitate the oxidation of remaining DNAN molecules. As shown in Fig. S5,† in the condensed phase, NO_2 generated from primary reactions can make a nucleophilic attack at the phenyl ring to generate NO. Consequently, the frequency of A + B type O transfer reactions increases by 100% (Table 2). In contrast, at 3500 K, the frequency of bimolecular H transfer reactions decreases due to their competition with bimolecular O transfer reactions.

Besides NO_X, CH_2O and H_2O are also produced in the initial decomposition of DNAN. At 2500 K, an H is transferred from the $^{\bullet}OCH_3$ produced from P6 to the nitro of another DNAN to form the first CH_2O at 57.1 ps (Fig. 8(a)). This is followed by the formation of the first H_2O at 58.5 ps (Fig. 8(b)). An intramolecular H transfer first occurs in INT7$_2$ produced from P7 leading to the formation of the $-NO_2H$ group, which further abstracts an H atom from the $-OCH_3$ group of another DNAN. The products include H_2O and $Ph(NO_2)_2$–OCH_2 and then the C_{phyl}–O bond of the latter is broken to release the second CH_2O.

3.2.2.2 Intermediate decomposition stage. In the DNAN intermediate decomposition stage in the condensed phase (Fig. 6), the system contains DNAN-dimer and monomer fragments, small molecules, and radicals. The second stage is characterized by reactions among primary products and the subsequent decomposition of benzene rings into carbon clusters. Fast generation of N_2, CO_2, H_2O, and H_2 is visible, accompanied by the depletion of NO_2, CH_2O, and NO (Fig. 9).

At 3500 K, CH_2O is almost completely consumed at the end of the second stage (Fig. 9(b)). CO is generated from CH_2O by dehydrogenation and is further oxidized to the more stable CO_2 (Fig. S6(a)†). When substitution groups fall off from DNAN, the remaining phenyl ring can also rupture to generate CO_2 (Fig. S6(b)†). However, the amount of CO_2 produced by the former is much greater than that by the latter. Alternatively, the remaining phenyl ring can also directly polymerize to form carbon clusters (Fig. S7†). The number of N–O bonds further decreases (Fig. S3†), because $H^{\bullet}$ radicals reduce NO_X to N_2, which also produces $OH^{\bullet}$. The combination of $OH^{\bullet}$ with $H^{\bullet}$ yields H_2O eventually. At the same time, C–O bonds form promptly due to the oxygen transfer from N to C. The increase in the numbers of N–N, O–H, and C–O bonds is also partially due to the formation of stable N_2, H_2O, and CO_2 molecules, respectively (Fig. S3†).

The DNAN decomposition rate constants in the intermediate stage are estimated by fitting the PE curve (Fig. 6) through eqn (3), and the calculated k_1 at 2500 and 3500 K are 0.013 and 0.059 ps^{-1}, respectively (Table 3). Small molecules, like NO_2, NO, and CH_2O, all vanish much faster at 3500 K than at 2500 K (Fig. 9). Then the pre-exponential factor A and activation energy E_a can be obtained from eqn (2), whose values are 2.59 ps^{-1} and

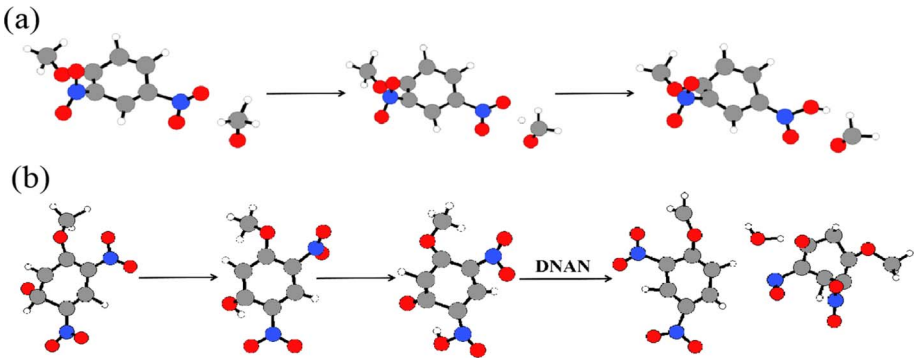

Fig. 8 The formation of the first CH_2O (a) and H_2O (b) at 57.1 and 58.5 ps, respectively, during the initial decomposition of DNAN in the condensed phase at 2500 K. The C, H, O, and N atoms are colored gray, white, red, and blue, respectively.

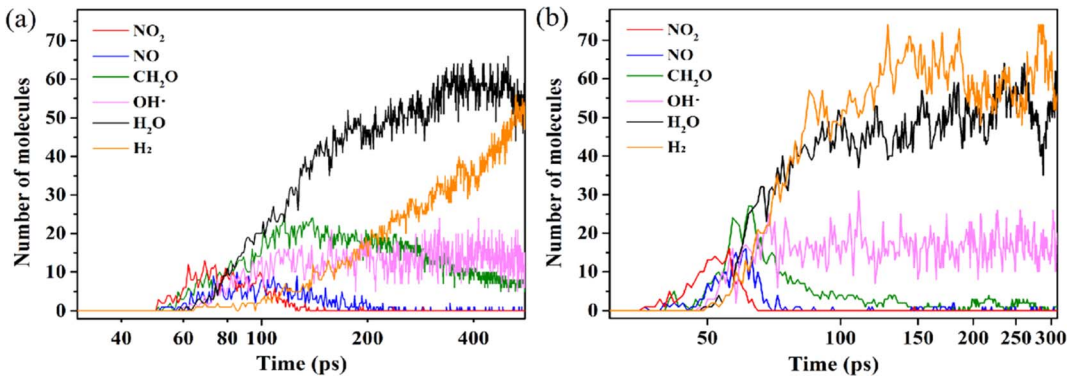

Fig. 9 The time evolution of the number of light intermediates from the DNAN decomposition at 2500 K (a) and 3500 K (b).

26.30 kcal mol^{-1} (Table 3), respectively, which reasonably agrees with the experimental value (19.15 ± 1.36 kcal mol^{-1}).[41]

3.2.2.3 Final product evolution stage. In our MD simulations, the final products from the thermal decomposition of DNAN at high temperatures include CO_2, N_2, H_2O, H_2, and carbon clusters containing some O, H, and N atoms (Fig. S8†). The amounts of stable gas products decrease in the order: of H_2O > N_2 > CO_2. At higher temperatures, more N_2 is formed since fewer N atoms are trapped in carbon clusters. Moreover, a large amount of H_2 is also generated (Fig. 9 and S8†) due to the severe negative oxygen balance of DNAN. Since the C=O bond energy is greater than the O–H bond energy, the O atom prefers to combine with C to form CO_2. Besides these small molecules, the decomposition of DNAN leads to the formation of the copious amount of large molecular clusters, containing mostly carbon atoms. These carbonaceous clusters start to form in the second stage of the DNAN decomposition and further grow in size afterward. At 3500 K, more heat is available for the ring-opening reactions to form larger carbon clusters with a maximum molar mass up to 3000 g mol^{-1}. These carbon clusters in DNAN capture a significant amount of O and, to a lesser extent, N atoms, suspending the formation of final gas-phase products. When most of the H_2O, CO_2, and N_2 molecules are formed, the energy release slows down. Then, carbon cluster residues begin to release O, H, and N atoms at a slower pace, while their C content gradually increases. A close inspection of the MD trajectories at the end of the decomposition identifies large $C_{150}H_{21}O_{64}N_{15}$ (Fig. S8(b)†) and $C_{175}H_{40}O_{63}N_{10}$ clusters at 2500 K and 3500 K, respectively.

The reaction rate constant k_2 for this stage is estimated by the reaction rate analysis method (Sec. 2.2.2). Effective rate constants for each product creation can be calculated from eqn (3). Simulated results are presented in Fig. 10 and Table 3. There is a good agreement between the simulated and fitted asymptotic amounts of all final gas products, indicating that the simulation reactions have reached equilibrium. As expected, the formation rates of all three final gas products increase with the temperature, and that of H_2O is the highest.

Table 3 Comparison of the kinetic parameters for DNAN decomposition at 2500 and 3500 K

				k_2/ps^{-1}		
T/K	k_1/ps^{-1}	A/ps^{-1}	E_a/kcal mol^{-1}	CO_2	N_2	H_2O
2500	0.013	2.59	26.30	0.0066	0.0062	0.0089
3500	0.059			0.011	0.011	0.012

3.3 Analysis of key reactions

The TG-FTIR-MS analysis reveals that among the various species produced by the initial thermal decomposition of DNAN, the

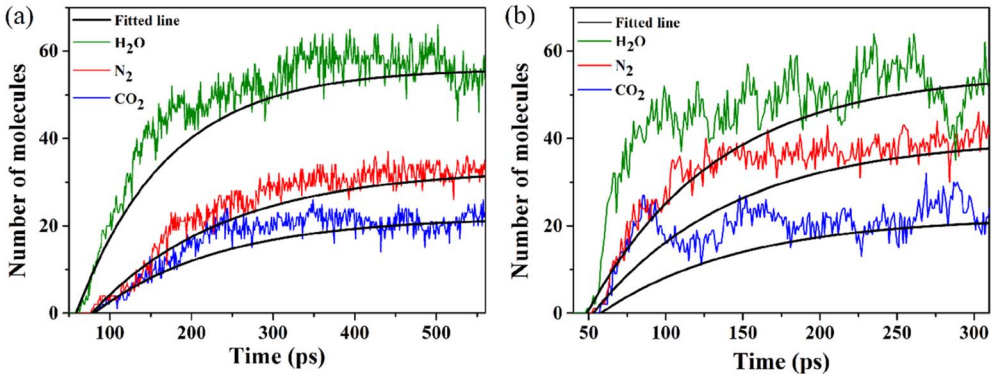

Fig. 10 Time evolution of the number of H_2O, N_2, and CO_2 products from the DNAN decomposition at 2500 K (a) and 3500 K (b). Black lines are the exponential fits.

amounts of NO and CH_2O are greater than that of NO_2, while the amount of $Ph(OH)_2OCH_3$ is greater than that of $Ph(OH)_3$ and far greater than that of $PhOCH_3$ (Fig. 3 and 4). The measured data can be rationalized by our MD simulations, which reveal that the initial decomposition stage is dominated by the unimolecular P1 and later by bimolecular P4 (NO_2 attacks the $-OCH_3$ group of DNAN) reactions (Fig. 5), and the NO_2 produced by P1 is deoxidized to NO by P4. Another source of NO is from P2 (Fig. 5(a)), the C–NO_2 rearrangement of DNAN. $Ph(OH)(OH_2)OCH_3^+$ ($m/z = 141$, 142) can be produced through P2 or P5. Due to its p–π conjugation with the phenyl ring, the reaction of $-OCH_3$ is more difficult than $-NO_2$. However, $-OCH_3$ can be knocked off through P4 or P6. P4 is more prone to occur than P6, as NO_2 is much more reactive than DNAN. The production of $Ph(OH)_3$ requires the $-OCH_3$ group and two nitro groups of a DNAN molecule to react away simultaneously, which is of low probability. This explains why the amount of $Ph(OH)_2$–OH_2^+ is relatively low in the TG-FTIR-MS analysis. Only a small amount of DNAN undergoes C–NO_2 homolysis in both *ortho* and *para* position, especially in the condensed phase, resulting in a low amount of $PhOCH_3$.

The *ortho*-NO_2 homolysis process of DNAN and TNT single molecules is further compared using the relaxed scan algorithm *via* DFT. As shown in Fig. 11(a), both pathways are barrierless, in accordance with the report[64] by Wang *et al.* For both molecules, the changes of PE are similar, 75.96 kcal mol^{-1} for TNT and 77.54 kcal mol^{-1} for DNAN. In contrast, the reaction barrier of the triggering α-H transfer of TNT is only 47.15 kcal mol^{-1} as shown in Fig. 11(b) and S9(c).†

The PE changes of bimolecular H or O transfer reactions for DNAN and TNT are computed *via* DFT and compared in Fig. 11(b). For DNAN bimolecular (A + A) reactions, the energy barriers are relatively high, 78.61 kcal mol^{-1} and 99.92 kcal mol^{-1} for inter-molecular H and O transfer, respectively. This explains why the frequencies of these bimolecular (A + A) reactions are low during the DNAN detonation (Table 2). However, after NO_2 radicals are produced from primary reactions, the reactions of DNAN become faster as the activation energy of bimolecular (A + B) O transfer reactions is significantly reduced to 25.52 kcal mol^{-1}. This is particularly favorable for DNAN decomposition in the gas phase since small radicals like NO_2 have greater mobility than those in a condensed phase. This explains the experimental observation in ref. 58 that the thermal decomposition of DNAN happens mostly in the gas phase when it is in vapor–liquid equilibrium.

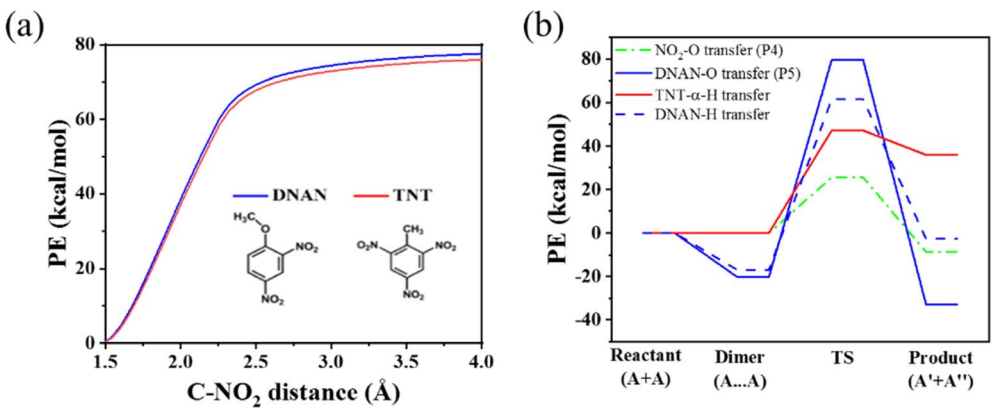

Fig. 11 The PE changes due to the release of *ortho*-NO_2 (a) and the O and H transfer (b) of the DNAN and TNT computed from DFT. The dimer, TS, and product structures of reactions in (b) are provided in Fig. S9.†

4. Conclusions

We combine the TG-FTIR-MS analysis, DFT, and RaxFF-lg MD calculations to investigate the thermal decomposition and detonation processes of DNAN. Based on the measured and computed results, the following conclusions are drawn:

(1) Due to the lack of α-H, the thermal decomposition of DNAN is triggered by unimolecular C–NO_2 homolysis at *ca.* 453 K, which produces active NO_2 radical for secondary reactions. The maximum reaction rate is reached at *ca.* 513 K, and gas products are NO, NO_2, CH_3OH and fragments containing the benzene moiety. The estimated activation energy from DFT computations is 77.54 kcal mol^{-1}, which is close to the measured one of 71.19 kcal mol^{-1}.

(2) Unlike the –CH_3 group of TNT, the –OCH_3 group of DNAN is significantly less reactive due to its p–π conjugation with the phenyl ring. Instead of C–O homolysis, the –OCH_3 group is mainly reacted by NO_2 attack. This reaction renders the decomposition of DNAN highly favorable especially in the gas phase due to its low energy barrier and high mobility of NO_2 radical.

(3) The detonation of DNAN in the condensed phase is dominated by bimolecular reactions and 37.5% of them are O transfer reactions, while 33.3% of them are H transfer reactions in our ReaxFF MD simulation at 2500 K. At 3500 K, the frequency of O transfer reactions increases, while that of H transfer reactions decrease. This is mainly due to the increase in the number of fragment radicals like NO_2 and their mobility, which is important for condensed-phase reactions.

(4) For the second stage of DNAN detonation, unstable intermediate species, like NO_X and CH_2O, are further converted to stable products, H_2O, CO_2, and N_2, and a large quantity of explosion heat is generated. Due to its poor O balance, C and H in DNAN cannot be fully oxidized. At the end of the reaction, there is a certain amount of H_2 and carbon clusters.

(5) The higher thermal stability and lower explosion heat of DNAN than TNT is attributed to several structural factors, *i.e.* the lack of α-H, inactive –OCH_3 group, and less nitro groups causing severe negative O balance.

(6) Our results provide explanation for the empirical E–P–S equation of polynitroaromatic explosives, whose activation energy is inversely proportional to the heat of explosion. Due to the higher activation energy of DNAN than TNT, less active radicals are produced during the initiation stage of the former' detonation. Consequently, the detonation heat of DNAN is lower than that of TNT.

Conflicts of interest

There are no conflicts to declare.

Acknowledgements

This research is funded by the National Natural Science Foundation of China [grant no. 12272184]. We thank Miss Ayesha Hina for proofreading the manuscript.

References

1 S. H. Kim, B. W. Nyanda, H. S. Kim, J. S. Park, W. J. Lee and M. Oh, Numerical analysis of thermal decomposition for RDX, TNT, and composition B, *J. Hazard. Mater.*, 2016, **308**, 120–130.
2 M. Anniyappan, M. B. Talawar, R. K. Sinha and K. P. S. Murthy, Review on advanced energetic materials for insensitive munition formulations, *Combust., Explos. Shock Waves*, 2020, **56**, 495–519.
3 E. B. F. Galante, N. Mai, M. K. Ladyman, P. P. Gill, T. J. Temple and F. Coulon, Evaluation of small-scale combustion of an insensitive high explosive formulation containing 3-nitro-1,2,4-triazol-5-one (NTO), 2,4-dinitroanisole (DNAN), and 1,3,5-trinitroperhydro-1,3,5-triazine (RDX), *J. Energ. Mater.*, 2021, **39**(1), 85–99.
4 J. S. Li, J. J. Chen, C. C. Hwang, K. T. Lu and T. F. Yeh, Study on thermal characteristics of TNT based melt-cast explosives, *Propellants Explos. Pyrotech.*, 2019, **44**(10), 1270–1281.
5 B. A. Steele, Initial decomposition mechanisms of 2,4,6-triamino-1,3,5-trinitrobenzene (TATB) and their kinetic isotope effect, *J. Appl. Phys.*, 2023, **133**, 075902.
6 C. L. Armstrong and J. T. Mang, Thermally-driven changes to porosity in TATB-based high explosives, *Propellants Explos. Pyrotech.*, 2021, **46**(8), 1304–1312.
7 S. R. Li, Z. P. Duan, T. Y. Gao, X. J. Wang, Z. C. Ou and F. L. Huang, Size effect of explosive particle on shock initiation of aluminized 2, 4-dinitroanisole (DNAN)-based melt-cast explosive, *J. Appl. Phys.*, 2020, **128**(12), 125903.
8 W. Zhang, L. Salvati, M. Akhtar and D. D. Dlott, Shock initiation and hot spots in plastic-bonded 1,3,5-triamino-2,4,6-trinitrobenzene (TATB), *Appl. Phys. Lett.*, 2020, **116**, 124102.
9 A. K. Burnham, V. L. Stanford, S. Vyazovkin and E. M. Kahl, Effect of pressure on TATB and LX-17 thermal decomposition, *Thermochim. Acta*, 2021, **699**, 178908.
10 B. D. Wu, J. Q. Zhou, Y. Y. Guo, R. Zhu, D. Wang, C. W. An and J. Y. Wang, Preparation of HMX/TATB spherical composite explosive by droplet microfluidic technology, *Def. Technol.*, 2023, **21**(3), 11.
11 D. S. Viswanath, T. K. Ghosh and V. M. Boddu, *Emerging Energetic Materials: Synthesis, Physicochemical, and Detonation Properties*, Springer, Dordrecht, the Netherlands, 2018.
12 P. J. Davies and A. Provatas, Characterisation of 2,4-dinitroanisole: an ingredient for use in low sensitivity melt cast formulations, *Defence Science and Technology organisation edinburgh (Australia) Weapons Systems Div*, 2006.
13 V. M. Boddu, K. Abburi, S. W. Maloney and R. Damavarapu, Thermophysical properties of an insensitive munitions compound, 2,4-dinitroanisole, *J. Chem. Eng. Data*, 2008, **53**(5), 1120–1125.
14 A. Provatas and C. Wall, Ageing of australian DNAN based melt-cast insensitive explosives. Propell, Explos, *Pyrotech*, 2016, **41**(3), 555–561.

15 S. Taylor, M. E. Walsh, J. B. Becher, D. B. Ringelberg, P. Z. Mannes and G. W. Gribble, Photo-degradation of 2,4-dinitroanisole (DNAN): an emerging munitions compound, *Chemosphere*, 2017, **167**, 193–203.

16 S. H. Sun, H. B. Zhang, J. J. Xu, S. M. Wang, C. H. Zhu, H. F. Wang, R. Q. Ding, Z. H. Yu and J. Sun, Two novel melt-cast cocrystal explosives based on 2,4-dinitroanisole with significantly decreased melting point, *Cryst. Growth Des.*, 2019, **19**, 6826–6830.

17 F. C. Miao, X. R. Zhang, L. Zhou, X. X. Wu, T. Jiang and R. T. Xing, Hugoniot and mie–grüneisen equation of state of unreacted 2,4-dinitroanisole (DNAN), *Int. J. Impact Eng.*, 2019, **134**, 103369.

18 F. Chen, Y. C. Liu, Y. Wang and Q. H. Zhang, Review on Melt-cast carrier explosives, *Chin. J. Energetic Mater.*, 2020, **28**(11), 1109–1119.

19 D. L. Zhu, Z. Lin, X. R. Zhang and R. T. Xing, Comparison of Comprehensive properties for DNAN and TNT-Based melt-cast explosives, *Chin. J. Energetic Mater.*, 2019, **27**(11), 923–930.

20 R. F. Liu, X. J. Wang, F. L. Huang and H. J. Huang, Macro-meso-scale cook-off simulations of DNAN-based melt-cast explosives, *Acta Armamentarii*, 2022, **43**, 287–296.

21 J. J. Meng, L. Zhou, T. T. Cao and Q. H. Wang, Research progress of 2,4-dinitroanisole-based melt-cast explosives, *Chin. J. Energetic Mater.*, 2020, **28**, 13–24.

22 S. R. Li, Z. P. Duan, T. Y. Gao, Z. C. Ou and F. L. Huang, Shock initiation characteristic of insensitive DNAN-based aluminized melt-cast explosives, *Chin. J. Energetic Mater.*, 2021, **29**, 88–95.

23 S. R. Li, Z. P. Duan, B. H. Zheng, G. Luo and F. L. Huang, Cylinder test and equation of state for DNAN-based aluminized melt-cast explosives, *Acta Armamentarii*, 2021, **7**, 1424–1430.

24 G. Y. Wang, S. W. Zhang, Z. H. Wang and Q. Z. Cui, Mechanical properties of DNAN/HMX melt-cast explosive, *AIP Adv.*, 2022, **12**(6), 065227.

25 J. J. Meng, L. Zhou, D. Y. Jin, S. T. Cao and Q. H. Wang, Rheological properties of DNAN/HMX melt-cast explosives, *Chin. J. Energetic Mater.*, 2018, **26**, 677–685.

26 H. Wu, Z. P. Duan, M. J. Bai and F. L. Huang, Small-scale cook-off experiments and simulations of DNAN-based aluminized explosives, *Chin. J. Energetic Mater.*, 2021, **29**, 414–421.

27 Z. Y. Deng, Y. Wang, G. Y. Qi and Q. H. Zhang, High-pressure structural stability and melting performance of α-2,4-dinitroanisole, *Energ. Mater. Front.*, 2021, **2**, 272–277.

28 F. C. Miao, D. D. Li, Y. F. Cheng, J. J. Meng and L. Zhou, Shock initiation experiments with modeling on a DNAN based melt-cast insensitive explosive, *Def. Technol.*, 2023, **32**, 655–662.

29 M. M. Zhang, H. X. Wang, X. J. Cui, B. B. Li, X. Q. Fang and Y. M. Luo, Effect of polymers on mechanical properties of DNAN and its melt-cast explosives, *Chin. J. Energetic Mater.*, 2023, **31**, 41–47.

30 S. M. Jing, Z. M. Jiang, Q. J. Jiao, Z. H. Li, Y. C. Liu and L. Yang, 3,5-difluoro-2,4,6-trinitroanisole: promising melt-cast insensitive explosives instead of TNT, *J. Energ. Mater.*, 2022, **40**(2), 206–217.

31 Y. Kou, X. L. Song, L. X. Liu, Y. Wang, C. L. Liu and K. G. Guo, Preparation and properties of DNAN/TNAZ lowest eutectic mixture, *Chin. J. Explos. Propellants*, 2020, **43**, 531–536.

32 J. C. Oxley, J. L. Smith, M. A. Donnelly, K. Colizza and S. Rayome, Thermal stability studies comparing IMX-101 dinitroanisole/nitroguanidine/NTO) to analogous formulations containing dinitrotoluene, *Propellants Explos. Pyrotech.*, 2016, **41**, 98–113.

33 N. Palka and M. Szala, Transmission and reflection terahertz spectroscopy of insensitive melt-cast high-explosive materials, *J. Infrared, Millim. Terahertz Waves*, 2016, **37**, 977–992.

34 D. Frem, A review on IMX-101 and IMX-104 melt-cast explosive: insensitive formulation for the next-generation munition systems, *Propellants Explos. Pyrotech.*, 2023, **48**(1), e202100312.

35 S. Taylor, E. Park, K. Bullion and K. Dontsova, Dissolution of three insensitive munitions formulations, *Chemosphere*, 2015, **119**, 342–348.

36 J. J. Meng, Z. Lin and F. C. Miao, Review of essential characteristics of 2,4-dinitroanisole, *Cent. Eur. J. Energ. Mater.*, 2023, **20**(1), 50–74.

37 X. L. Xing, F. Q. Zhao, S. N. Ma, K. Z. Xu, L. B. Xiao, H. X. Gao, T. An and R. Z. Hu, Specific heat capacity, thermal behavior, and thermal hazard of 2,4-dinitroanisole, *Propellants, Explos. Pyrotech.*, 2012, **37**(2), 179–182.

38 W. A. Trzciński, S. Cudziło, S. Dyjak and M. Nita, A comparison of the sensitivity and performance characteristics of melt-pour explosives with TNT and DNAN binder, *Cent. Eur. J. Energ. Mater.*, 2014, **11**(3), 443–455.

39 R. Liu, T. L. Zhang, Z. N. Zhou and L. Yang, Volatilization interference in thermal analysis and kinetics of low-melting organic nitro compounds, *RSC Adv.*, 2014, **4**(19), 9810–9818.

40 C. Y. Zhang, S. H. Jin, J. W. Ji, B. C. Jing, F. Bao, G. Y. Zhang and Q. H. Shu, Thermal hazard assessment of TNT and DNAN under adiabatic condition by using accelerating rate calorimeter (ARC), *J. Therm. Anal. Calorim.*, 2018, **131**, 89–93.

41 R. X. Zhang, J. M. Gao, J. L. Wang, Y. L. Zhu, H. X. Pan and L. Z. Chen, Evaluation of thermal hazards based on thermokinetic parameters of 2,4-dinitroanisole, *J. Energ. Mater.*, 2022, **40**(4), 471–485.

42 J. F. Wang, S. S. Chen, S. H. Jin, Q. H. Shu, F. L. Huang, J. Ruan, X. Ma and K. Chen, Thermal hazard assessment of TKX-50-based melt-cast explosive, *Def. Technol.*, 2022, **18**, 1546–1551.

43 T. Ma, L. Jiang, X. L. Wu, Z. X. Han, N. Yang, Y. M. Luo and S. Xu, Theoretical and experimental studies on thermostatic explosion behavior of typical melting and casting explosive 2,4-dinitroanisole (DNAN), *Case Stud. Therm. Eng.*, 2023, **47**, 103043.

44 D. N. Shi, L. Z. Chen, J. L. Wang, J. Chen and H. X. Pan, Thermal properties study of low-melting-point-DNAN and

analysis of solidification behavior of high-melting-point-DNAN, *Propellants Explos. Pyrotech.*, 2021, **46**, 1–7.

45 H. Wang, Q. H. Wang, W. B. Huang, Y. M. Luo and H. X. Wang, Shock sensitivity of DNTF reduced by using DNAN, *Chin. J. Energetic Mater.*, 2010, **18**(4), 435–438.

46 J. J. Sabatini and K. D. Oyler, Recent advances in the synthesis of high explosive materials, *Crystals*, 2015, **6**(1), 5–26.

47 H. J. Li, Z. Zhang, N. Ma, S. Chen, H. J. Li, L. Yang, C. Y. Liang, J. H. Yi and F. Q. Zhao, Scaled-up production and quality controlling techniques of energetic cocrystals: challenges and prospects, *J. Phys.: Conf. Ser.*, 2023, **2478**(3), 032066.

48 C. Xiao, Q. Yu, X. Y. Zheng, B. H. Zheng, Y. Guo, G. Luo, B. Jin and J. S. Li, High-performance and insensitive DNTF-DFTNAN eutectic: binary phase diagram and characterization, *Propellants Explos. Pyrotech.*, 2022, **47**(11), e202200166.

49 D. F. Wang, L. Yang and W. H. Zhu, Effects of cocrystallization on the structure and properties of melt-cast explosive 2,4-dinitroanisole: a computational study, *Molecules*, 2022, **27**, 9010–9024.

50 S. H. Sun, H. B. Zhang, J. J. Xu, S. M. Wang, C. H. Zhu, H. F. Wang, R. Q. Ding, Z. H. Yu and J. Sun, Two novel melt-cast cocrystal explosives based on 2,4-dinitroanisole with significantly decreased melting point, *Cryst. Growth Des.*, 2019, **19**, 6826–6830.

51 J. J. Meng, Y. M. Luo, G. T. Niu, H. X. Wang and F. Yang, Effect of additives on the interface binding strength of DNAN/HMX melt-cast explosives, *J. Energ. Mater.*, 2020, **38**(4), 467–482.

52 S. Zeman, Study of chemical micro-mechanism of the energetic materials initiation by means of characteristics of their thermal decomposition, *The 34th NATAS Annual Conference*, 2006, pp. 7–9.

53 S. Zeman, Sensitivity of high energy compounds, *High Energy Density Materials Structure & Bonding*, T. Klapoetke, ed. New York, 2007, vol. 125, pp. 195–271.

54 S. Zeman and M. Jungova, Sensitivity and performance of energetic materials, *Propellants, Explos., Pyrotech.*, 2016, **41**, 426–451.

55 S. Zeman, Modified Evans–Polanyi–Semenov relationship in the study of chemical micro-mechanism governing detonation initiation of individual energetic materials, *Thermochim. Acta*, 2002, **384**, 137–154.

56 S. Zeman, Q. L. Yan and A. Elbeih, Recent advances in the study of the initiation of energetic materials using the characteristics of their thermal decomposition. Part II. Using simple differential thermal analysis, *Cent. Eur. J. Energ. Mater.*, 2014, **11**(3), 285–294.

57 S. Zeman, Characteristics of thermal decomposition of energetic materials in a study of their initiation reactivity, *Handbook of Thermal Analysis and Calorimetry*, Elsevier Science BV, 2018, vol. 6, pp. 573–612.

58 R. Liu, Dynamic pressure-measuring thermal analysis technique and applications, Doctoral dissertation, Beijing Institute of Technology, China, 2015.

59 A. Benhammada and D. Trache, Thermal decomposition of energetic materials using TG-FTIR and TG-MS: a state-of-the-art review, *Appl. Spectrosc. Rev.*, 2020, **55**(8), 724–777.

60 S. A. EL-Sayed, Review of thermal decomposition, kinetics parameters and evolved gases during pyrolysis of energetic materials using different techniques, *J. Anal. Appl. Pyrolysis*, 2022, **161**, 105364.

61 G. C. Lan, J. Li, G. Y. Zhang, J. Ruan, Z. Y. Lu, S. H. Jin, D. L. Cao and J. L. Wang, Thermal decomposition mechanism study of 3-nitro-1,2,4-triazol-5-one (NTO): combined TG-FTIR-MS techniques and ReaxFF reactive molecular dynamics simulations, *Fuel*, 2021, **295**, 120655.

62 H. Yao, L. Ni, P. H. Wu, J. C. Jiang, Y. Q. Ni and X. Y. Yao, Thermal hazard and pyrolysis mechanism of tetrazolo[1,5-a]pyridine by TG, DSC, ARC, TG-MS and DFT methods, *J. Anal. Appl. Pyrolysis*, 2021, **159**, 105299.

63 J. Wojtas and M. Szala, Thermally enhanced FTIR spectroscopy applied to study of explosives stability, *Measurement*, 2021, **184**, 110000.

64 K. Wang, B. Xue, J. G. Chen, Z. H. He, Y. P. Ji, B. Z. Wang, J. Lu, Z. W. Liu and Z. T. Liu, A combined experimental and theoretical study of the thermal decomposition mechanism and kinetics of ammonium dinitramide (ADN), *New J. Chem.*, 2020, **44**(17), 6833–6844.

65 S. Yousef, J. Eimontas, N. Striūgas, A. Mohamed and M. A. Abdelnaby, Pyrolysis kinetic behavior and TG-FTIR-GC–MS analysis of end-life ultrafiltration polymer nanocomposite membranes, *Chem. Eng. J.*, 2022, **428**, 131181.

66 Y. Guo, N. N. Zhao, T. Zhang, H. J. Gong, H. X. Ma, T. An, F. Q. Zhao and R. Z. Hu, Compatibility and thermal decomposition mechanism of nitrocellulose/Cr_2O_3 nanoparticles studied using DSC and TG-FTIR, *RSC Adv.*, 2019, **9**(7), 3927–3937.

67 S. P. Maharrey, D. Wiese-Smith, A. M. Highley, R. Behrens and J. J. Kay, *Interactions between ingredients in IMX-101: reactive chemical processes control insensitive munitions properties*, Sandia National Lab. (SNL-CA), Livermore, CA (United States), 2014.

68 Z. Mei, C. F. Li, F. Q. Zhao, S. Y. Xu and X. H. Ju, Reactive molecular dynamics simulation of thermal decomposition for nano-AlH_3/TNT and nano-AlH_3/CL-20 composites, *J. Mater. Sci.*, 2019, **54**, 7016–7027.

69 A. C. T. van Duin, S. Dasgupta, F. Lorant and W. A. Goddard, ReaxFF: a reactive force field for hydrocarbons, *J. Phys. Chem. A*, 2001, **105**(41), 9396–9409.

70 T. T. Zhou, H. J. Song, Y. Liu and F. L. Huang, Shock initiated thermal and chemical responses of HMX crystal from ReaxFF molecular dynamics simulation, *Phys. Chem. Chem. Phys.*, 2014, **16**(27), 13914–13931.

71 O. V. Sergeev and A. V. Yanilkin, Hydrogen transfer in energetic materials from ReaxFF and DFT calculations, *J. Phys. Chem. A*, 2017, **121**(16), 3019–3027.

72 A. Lele, H. Kwon, K. Ganeshan, Y. Xuan and A. C. T. van Duin, ReaxFF molecular dynamics study on pyrolysis of bicyclic compounds for aviation fuel, *Fuel*, 2021, **297**, 120724.

73 H. R. Zhang, X. X. Zhang, X. L. Fu, J. P. Liu, X. F. Qi and Q. L. Yan, Decomposition mechanisms of insensitive 2D energetic polymer TAGP using ReaxFF molecular dynamics simulation combined with Pyro-GC/MS experiments, *J. Anal. Appl. Pyrolysis*, 2022, **162**, 105453.

74 L. P. Jiang, X. L. Fu, Z. Y. Zhou, C. M. Zhang, J. Z. Li, F. Qi, X. Z. Fan and G. F. Zhang, Study of the thermal decomposition mechanism of FOX-7 by molecular dynamics simulation and online photoionization mass spectrometry, *RSC Adv.*, 2020, **10**(36), 21147–21157.

75 X. L. Duan, G. L. Jin, L. Y. Zhang, Z. S. Xu, R. X. Zhang and J. L. Wang, Insight into the pyrolysis of 3, 7-dinitro-1, 3, 5, 7-tetraazabicyclo [3, 3, 1] nonan (DPT) based on ReaxFF MD simulations and TG-FTIR-MS techniques, *Fuel*, 2023, **331**, 125860.

76 L. C. Liu, Y. Liu, S. V. Zybin, H. Sun and W. A. Goddard III, ReaxFF-lg: correction of the ReaxFF reactive force field for london dispersion, with applications to the equations of state for energetic materials, *J. Phys. Chem. A*, 2011, **115**(40), 11016–11022.

77 H. Liu, X. Dong and H. Y. H. Y, Reactive Molecular dynamics simulations of carbon-containing clusters formation during pyrolysis of TNT, *Acta Phys.-Chim. Sin.*, 2014, **30**(2), 232–240.

78 J. W. Meng, S. H. Zhang, R. J. Gou, Y. H. Chen, Y. Li, M. H. Chen and Z. Li, The thermal decomposition process of composition B by ReaxFF/lg force field, *J. Mol. Model.*, 2020, **26**, 1–11.

79 B. S. C. Nyburg, C. H. Faerman, L. Prasad, D. Palleros and N. Nudelman, Structures of 2,4-dinitroanisole and 2,6-dinitroanisole, *Acta Crystallogr., Sect. C: Cryst. Struct. Commun.*, 1987, **43**(4), 686–689.

80 R. M. Vrcelj, J. N. Sherwood, A. R. Kennedy, H. G. Gallagher and T. Gelbrich, Polymorphism in 2-4-6 trinitrotoluene, *Cryst. Growth Des.*, 2003, **3**(6), 1027–1032.

81 F. Guo, X. L. Cheng and H. Zhang, Reactive molecular dynamics simulation of solid nitromethane impact on (010) surfaces induced and nonimpact thermal decomposition, *J. Phys. Chem. A*, 2012, **116**(14), 3514–3520.

82 L. Chen, H. Q. Wang, F. Q. Wang, D. S. Geng, J. Y. Wu and J. Y. Lu, Thermal decomposition mechanism of 2,2′,4,4′,6,6′-hexanitrostilbene by ReaxFF reactive molecular dynamics simulations, *J. Phys. Chem. C*, 2018, **122**(34), 19309–19318.

83 T. T. Zhou, Y. D. Shi and F. L. Huang, Thermal decomposition mechanism of β-HMX under high pressures via ReaxFF reactive molecular dynamics simulations, *Acta Phys.-Chim. Sin.*, 2012, **28**(11), 2605–2615.

84 S. F. Zhu, R. Zhu, S. H. Zhang, C. W. Luo, S. B. Feng and G. R. Liu, ReaxFF/lg simulation on the substituent effect upon the thermal decomposition mechanism of nitrobenzene compounds, *Chin. J. Explos. Propellants*, 2023, **46**, 411–418.

85 W. J. Li, X. Zhang, R. Q. Liu, S. Y. Xu, S. Xu, Y. H. Lan, Y. Z. Fu, Y. Zhang, Y. G. Feng and W. G. Cao, Thermal decomposition, flame propagation, and combustion reactions behaviours of stearic acid by experiments and molecular dynamic simulation, *Chem. Eng. J.*, 2023, **461**, 141906.

86 M. J. Frisch, G. W. Trucks, H. B. Schlegel, G. E. Scuseria, M. A. Robb and J. R. Cheeseman, *Gaussian 09 Revision A.1*, Gaussian. Inc., Wallingford CT, 2009.

87 M. Walker, A. J. A. Harvey, A. Sen and C. E. H. Dessent, Performance of M06, M06-2X, and M06-HF Density Functionals for Conformationally Flexible Anionic Clusters: M06 Functionals Perform Better than B3LYP for a Model System with Dispersion and Ionic Hydrogen-Bonding Interactions, *J. Phys. Chem. A*, 2013, **117**(47), 12590–12600.

88 N. Rom, B. Hirshberg, Y. Zeiri, D. Furman, S. V. Zybin, W. A. Goddard and R. Kosloff, First-Principles-Based Reaction Kinetics for Decomposition of Hot, Dense Liquid TNT from ReaxFF Multiscale Reactive Dynamics Simulations, *J. Phys. Chem. C*, 2013, **117**(41), 21043–21054.

89 H. Liu, Y. H. He, J. L. Li, Z. X. Zhou, Z. X. Ma, S. Liu and X. Dong, ReaxFF molecular dynamics simulations of shock induced reaction initiation in TNT, *AIP Adv.*, 2019, **9**(1), 015202.

90 R. Cohen, Y. Zeiri, E. Wurzberg and R. Kosloff, Mechanism of thermal unimolecular decomposition of TNT (2,4,6-Trinitrotoluene): a DFT study, *J. Phys. Chem. A*, 2007, **111**(43), 11074–11083.

91 E. V. Nikolaeva, D. V. Chachkov, A. G. Shamov and G. M. Khrapkovskii, Alternative mechanisms of thermal decomposition of O-nitrotoluene in the gas phase, *Russ. Chem. Bull.*, 2018, **67**, 274–281.

92 M. Yang, C. Y. Liao, C. L. Tang, P. Zhang, Z. H. Huang and J. L. Li, Theoretical studies on the initial reaction kinetics and mechanisms of *p*-, *m*- and *o*-nitrotoluene, *Phys. Chem. Chem. Phys.*, 2021, **23**(8), 4658–4668.

93 Z. H. He, J. Chen and Q. Wu, Initial decomposition of condensed-phase 1,3,5-triamino-2,4,6-trinitrobenzene under shock loading, *J. Phys. Chem. C*, 2017, **121**(15), 8227–8235.